

# Absence of selection for quantum coherence in the Fenna-Matthews-Olson complex: a combined evolutionary and excitonic study

Stéphanie Valteau,<sup>1</sup> Romain A. Studer,<sup>2</sup> Florian Häse,<sup>1</sup> Christoph Kreisbeck,<sup>1</sup> Rafael G. Saer,<sup>3</sup> Robert E. Blankenship,<sup>3</sup> Eugene I. Shakhnovich,<sup>1</sup> and Alán Aspuru-Guzik<sup>1</sup>

<sup>1</sup>*Department of Chemistry and Chemical biology,  
Harvard University, Cambridge, MA, 02138, USA.\**

<sup>2</sup>*European Bioinformatics Institute (EMBL-EBI),  
Wellcome Genome Campus, Hinxton, Cambridge, CB10 1SD, UK.*

<sup>3</sup>*Departments of Biology and Chemistry, Washington University in Saint Louis,  
One Brookings Drive, St. Louis, Missouri 63130 United States*

We present a study on the evolution of the Fenna-Matthews-Olson bacterial photosynthetic pigment-protein complex. This protein complex functions as an antenna. It transports absorbed photons —excitons— to a reaction center where photosynthetic reactions initiate. The efficiency of exciton transport is therefore fundamental for the photosynthetic bacterium’s survival. We have reconstructed an ancestor of the complex to establish whether coherence in the exciton transport was selected for or optimized over time. We have also investigated on the role of optimizing free energy variation upon folding in evolution. We studied whether mutations which connect the ancestor to current day species were stabilizing or destabilizing from a thermodynamic view point. From this study, we established that most of these mutations were thermodynamically neutral. Furthermore, we did not see a large change in exciton transport efficiency or coherence and thus our results predict that exciton coherence was not specifically selected for.

The Fenna-Matthews-Olson complex is a light-harvesting protein complex found in green sulfur bacteria. These bacteria first appeared about 1.6 billion years ago, in the Proterozoic era [1]. Green sulfur bacteria survive through anoxygenic photosynthesis; they use sulfide and other reduced sulfur compounds or hydrogen as photosynthetic electron donors [2].

In the last decade, much research has been dedicated to understanding the excitation energy transfer in the Fenna-Matthews-Olson (FMO) protein complex [3–13]. Once absorbed, photons become molecular excitations, or excitons. These excitons are then transported through the complex due to their interactions with neighboring excitations, the protein scaffold and the environment. A renewed interest in this complex arose when low temperature 2D-spectroscopy experiments suggested the presence of quantum coherence effects [14, 15] in the exciton dynamics. Quantum coherent effects can be thought of as concurrent beats between electronic excitations which do not occur classically. Following these experiments, much theoretical work was carried out [6, 16–19] with the goal of understanding whether quantum effects were present and if so, how they contributed to the exciton transport. Most of the studies have relied on the existence of an X-ray crystal structure of the FMO complex of either *Chlorobaculum tepidum* or *Prosthecochloris aestuarii*.

FMO is found in all of the anaerobic Chlorobi phyla and recently it has also been found in aerobic *Chloracidobacterium thermophilum* of the Acidobacteria phyla [20]. In these organisms, the FMO complex forms a homo trimer (see Fig. 1). Each monomer consists of 7/8

bacteriochlorophyll-a (BChl-a) pigment molecules enclosed in a protein scaffold. The BChl pigment molecules interact with the protein scaffold through coordination and hydrogen bonds. The complex is thought to act as an excitonic wire, funneling the excitation from the baseplate to the reaction center where charge separation occurs. This charge separation enables reactions which are fundamental to the organisms’ survival. The biological origin of the complex remains a mystery. Olson et al. (Ref. [21]) speculated that the FMO complex might have come from an ancient reaction center. They looked for homology between the FMO protein and PscA, the reaction center protein of green sulfur bacteria. They found a signature sequence common to both, however the sequences only had a 13% identity score. More recently, the role of some specific site mutations [22] and of cysteines in the FMO protein has been investigated as well [23]. In Ref. [23] it was found that cysteines appear to be fundamental for the photoprotection mechanism of the protein complex.

Regarding exciton transport in this system, there have only been few efforts to understand whether and how protein evolution might have influenced it. For instance, in Ref. [24], the authors computed the BChl transition energies and looked at the effect of including the point charges coming from the protein. They also looked at how changes in the polar groups of amino acids, such as the amino or hydroxyl groups, influence BChl transition energies. They found that the charges coming from the alpha helices seem to influence the energies strongly. On the other hand, no large change in the energies was observed when they modified the charge distribution of single amino acids as a means to emulate single point mutations. Experimentally, the Blankenship group [25] looked at comparing the optical properties of FMO com-

\* svalteau@fas.harvard.edu

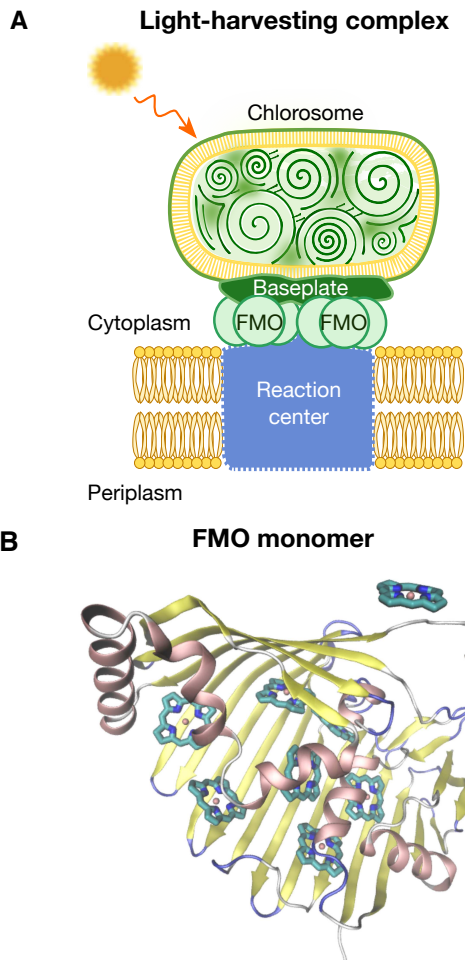


Figure 1. In panel **A**, an image describes the location of the FMO complex in the light-harvesting complex of green sulfur bacteria. The photons are absorbed by the chlorosome and transported as excitations to the FMO complex and ultimately to the reaction center. In panel **B** one can see crystal structure of FMO complex monomer for *Chlorobaculum tepidum* (PDB: 3ENI). The protein scaffold is colored in pink for alpha helices, in yellow for beta sheets, and in blue for loops. The 8 bacteriochlorophyll-a (BChl-a) pigments are colored in cyan (their side chains are not shown for simplicity).

ing from three different species to understand the effect of the protein scaffold. They observed spectral differences, and these were assigned to the way the BChl molecules bind to the protein scaffold in each species. This suggests that one may probe exciton dynamics and the biological role of coherence through point mutations. In this sense, we are most interested in mutations occurring in the vicinity of BChl binding sites as the effect of their charge is expected to have a stronger influence on the BChl energies.

For the above reasons, we have carried out a theoretical study of the protein complex from an evolutionary perspective. We aimed to identify whether quantum coher-

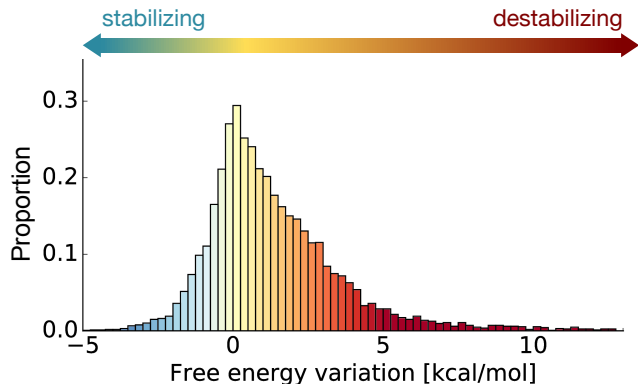


Figure 2. Histogram of free energy variation upon folding,  $\Delta\Delta G = \Delta G_{mutant}^{fold} - \Delta G_{wild}^{fold}$ , for all possible single-point mutations in the FMO complex trimer of *P. aestuarii* (PDB: 3EOJ). The coloring is shaded to be more red for destabilizing mutations (positive values) and blue for stabilizing mutations (negative values). The bins in the histogram are normalized by the area under the histogram.

ence in exciton transport and thermodynamic stability (free energy change upon folding) guided the evolution of the protein complex. Hence, we carried out calculations which trace evolution of exciton transport as well as evolution of thermodynamic stability. For the thermodynamics, we studied the stability of the current day protein complex to mutations by computing and comparing the folding free energies due to point mutations along the phylogenetic tree. Thus, with these two results, we were able to compare the stability of *C. tepidum* to the stability of its ancestors and see how it changed along the tree. To investigate on role of exciton transport, we computed and compared exciton transport in the ancestor with that of *C. tepidum*. Because two-dimensional photon echo (2D-echo) spectroscopy is the experimental tool employed to reveal coherent phenomena, we computed this spectrum to determine the role of coherence in the evolution from ancestor to *C. tepidum*. Finally, from the reconstructed phylogenetic tree, we identified sites under positive selection and determined whether positively selected amino acids were close to BChl molecules and could influence exciton transport.

## RESULTS

### Robustness of current day FMO proteins to mutations

We computed the free energy change upon folding,  $\Delta\Delta G = \Delta G_{mutant}^{fold} - \Delta G_{wild}^{fold}$ , as a measure of robustness of the FMO complex to mutations. Calculations were carried out using FoldX [26] for the trimers of *C. tepidum*

and *P. aestuarii* for all possible single point mutations (see Methods for details). In our model, each single point mutation occurs at the same time in all monomers of the trimer. We found that most single point mutations would be destabilizing  $\sim 60\%$  (see Fig. 2). The overall landscape of mutations is the same for *C. tepidum* and *P. aestuarii* (see Fig. S2 in the Supporting Information). This is qualitatively similar to the general statistics of the effects of mutations on stability (see Ref. [27, 28]).

We also looked at how the free energy change varies depending on the location of the mutation in the protein complex monomers of *P. aestuarii* and *C. tepidum* and found that mutations at the interface of monomers are among the most destabilizing (see Fig. S3). These observations rely on the assumption that each single point mutation (in each monomer) does not impede the assembling of a trimeric structure.

### Ancestor reconstruction, selection of mutations and variation of the free energy landscape

A phylogenetic tree was generated using the multiple sequence alignment built from the *fmoA* amino acid sequences (see details in Methods). The amino acid sequences were obtained by translating the *fmoA* monomer gene sequences. In Fig. 3 we show the cladogram tree (phylogenetic tree is also shown in Fig. S1). The tree divides in two main clades: saltwater (e.g. *P. aestuarii*) and freshwater (e.g. *C. tepidum*) bacteria.

At each node of the tree, the sequence and structure of the protein scaffold were reconstructed. The ancestral amino acid sequences were obtained using Bayesian inference and the scaffold structures were computed using homology modeling (see Methods). The pie-charts above each branch indicate, based on the diameter, how many mutations occurred between the two branch nodes, and based on the color, whether they were stabilizing (blue), neutral (grey) or destabilizing (red). Most mutations were neutral in terms of modifying the free energy change upon folding.

Given the inferred ancestor amino acid sequence at the root we constructed a guess for the full ancestral structure (protein scaffold and BChl molecules) through a combination of homology modeling and molecular dynamics simulations (see Methods). An image of the structure of the putative ancestor compared to that of *C. tepidum* for one monomer is shown in Fig. 4. The images in each panel are constructed from a snapshot of the molecular dynamics simulations at 300K after equilibration. In panel B, we show two orientations of one monomer of the protein complex. No large difference in the backbone of the protein is observed. This is due to the fact that the protein scaffold was constructed with homology modelling. The differences come from the location of side chains and the change in charge of the mutated amino acids. In panel B, mutations are highlighted using a color scheme based on the BLOSUM90 distance.

We see a few red mutations (large negative BLOSUM90 distance) on the beta sheet which could be a problem for the formation of the trimer. Another effect of the mutations is the change in orientation of BChl molecules (see Panel A). This change in orientation of the BChls influences the coupling amongst their first excited states (see Table S1). In particular, the coupling between the first excited states of BChl 3 and 4 is weaker in the ancestor than in *C. tepidum* and, on the other hand, the coupling between the first excited states of BChl 4 and 5 is stronger in the ancestor than it is in *C. tepidum*. Finally, as can be seen in Tab. S2, the average distance of the amino acids from the BChl molecules changes between the ancestor and *C. tepidum* and the differences are on the order of 0.1-0.4Å.

Given the phylogenetic tree, we also identified branches under positive selection (bright green) by using the branch-site model (details in Methods). In Fig. 5, we show mutations which were positively selected for along these branches in the structure of *C. tepidum*. Most positively selected mutations are distant from the BChl residues, and therefore we currently do not believe they had a strong role in modifying exciton transport. Given the high computational cost associated with constructing the full structure (with BChl molecules) at each node, we did not investigate the role of each positively selected mutation using atomistic *ab initio* methods. However, we computed the free-energy changes associated with the mutations.

In Fig. 6, panel A, we show the histogram of free energy changes which connects the ancestor to current day species in red and, in cyan, the histogram of folding free energy variation for all possible single-point mutations in the FMO complex trimer of *C. tepidum*. We found that 65% of mutations are destabilizing for *C. tepidum*. On the other hand only 32% of mutations of the ancestral FMO complex along the phylogenetic tree were destabilizing while 21% were stabilizing and 47% were neutral. This could indicate that mutations which favored the folding free energy change variation during evolution led to more stable current day protein structures. However, we cannot claim this in general as the trend changes for different current day species. For instance, as can be seen by comparing the two figures in panel B of Fig. 6, the distribution of folding free energy changes for mutations which connect the ancestor to *P. aestuarii* is significantly different from that for mutations which connect the ancestor to *C. tepidum*. This difference was confirmed by the Kolmogorov-Smirnov test. Furthermore, we computed that, for the mutations which connect the ancestor to *P. aestuarii*, 25 % are stabilizing and 19% are destabilizing. However, in the case of mutations which lead to *C. tepidum*, 47% are destabilizing while 22% are stabilizing. This indicates that *C. tepidum* is less stable than the ancestor while *P. aestuarii* is more stable than the ancestor.

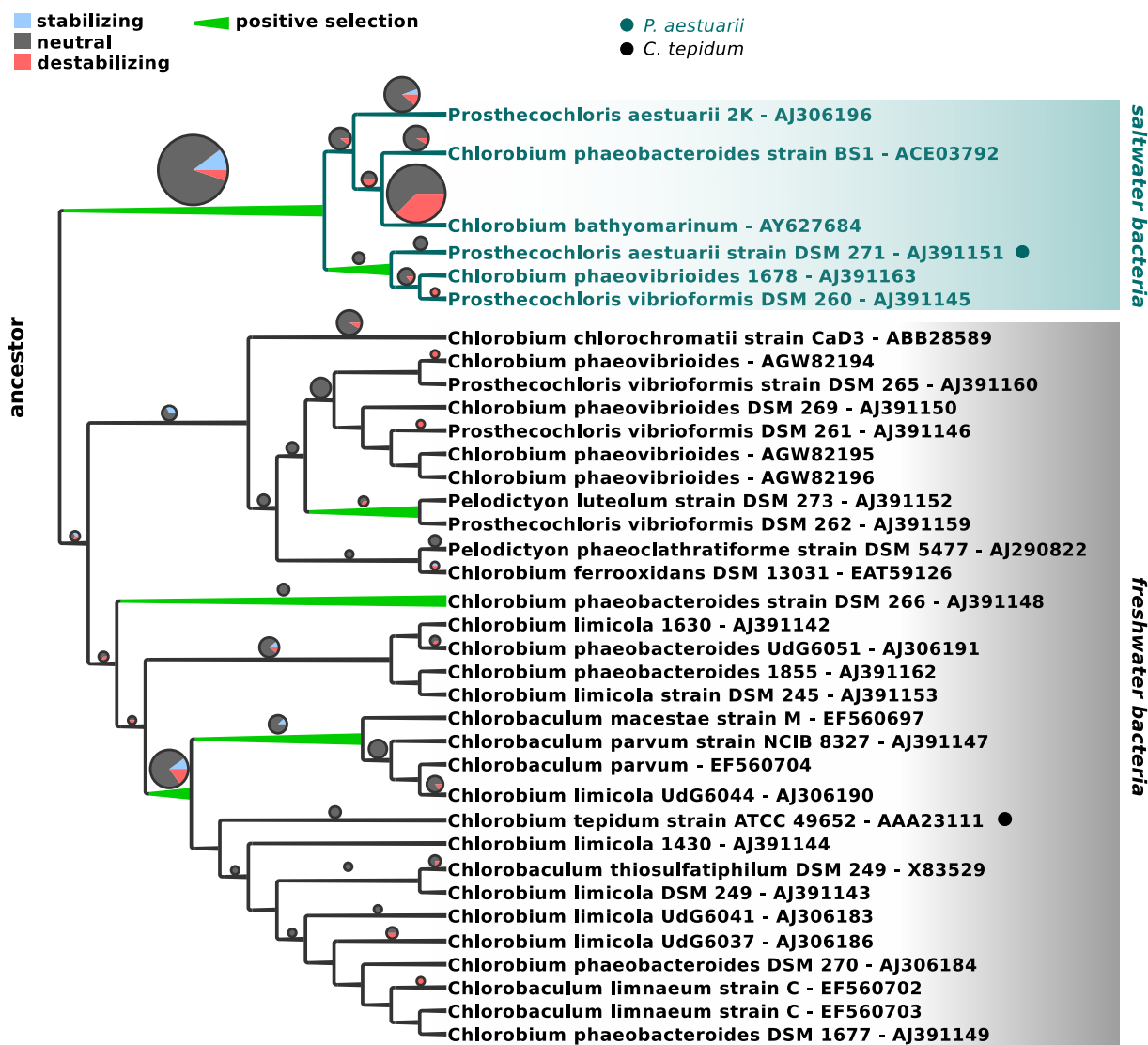


Figure 3. Rooted cladogram for *fmoA* computed using MAFFT and TranslatorX [29] for the alignment and PHYML [30]. Above each branch we show a pie-chart label with a diameter proportional to the number of single point mutations and color based on the associated free energy change  $\Delta\Delta G$ . Red represents destabilizing mutations, blue represents stabilizing mutations, and grey represents neutral mutations.

## Exciton transport and coherence

### Absorption, circular dichroism and linear dichroism

In Fig. 7 we compare the absorption spectrum of the ancestor to that of *C. tepidum*. The ancestor spectrum shows three main absorption peaks at 807, 819 and 830 nm while *C. tepidum* shows strong absorption at 804, 814 and 826 nm. These trends and the corresponding circular dichroism spectra (see Supporting Information) of the ancestor and of *C. tepidum* are very similar, respectively, to the spectra of FMO in *C. thiosulfatophilum* and *C. limicola* reported in Ref. [31]. However, we do not see

strong evidence of a similarity between the ancestor spectrum and the reaction center absorption spectra reported in that work. The small bump at about 845 nm (see Fig. 7) is most likely due to noise, as it does not correspond to any of the frequencies of the equivalent Fermi-Golden rule absorption spectrum. Therefore, our current results do not confirm that the ancestor is related to current day PscA, the reaction center protein of green sulfur bacteria, however we cannot exclude that it may have been related to ancestral reaction centers.

In the Supporting Information we also show the comparison of our *C. tepidum* spectra to the experimental absorption, linear dichroism and circular dichroism spec-

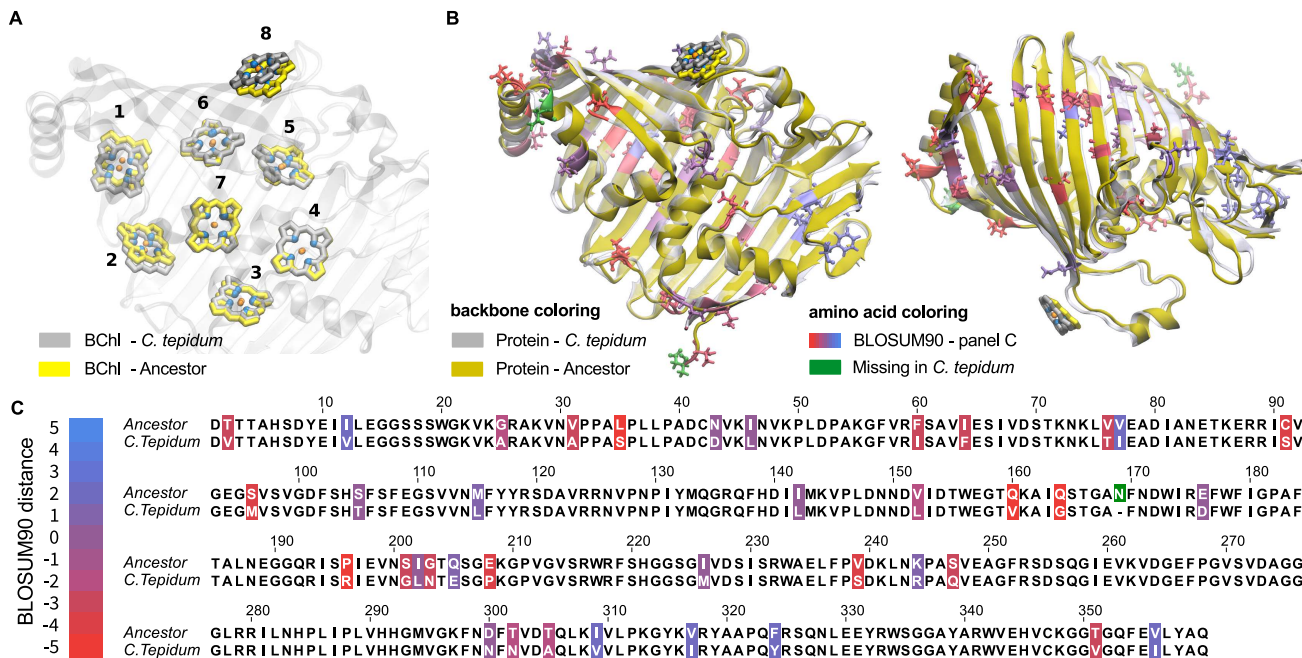


Figure 4. In panel **A**, we show the structure of the BChl molecules in a monomer of the ancestral structure (yellow) overlaid with the BChl molecules in the current day structure of *C. tepidum* (light grey). The images were generated from snapshots of the molecular dynamics simulations at 300K. In panel **B**, for the same snapshots we compare the backbone of the ancestral FMO structure (yellow) to that of the current day *C. tepidum* structure (light grey backbone). Some amino acids are colored based on the BLOSUM90 matrix, which quantifies how different they are (positive numbers indicate easy substitution while negative numbers indicate difficult substitution). These amino acids are also highlighted in the legend in panel **C**. The structures are snapshots from the molecular dynamics simulations at 300K. The amino acids which differ in the two structures are colored based on the BLOSUM90 matrix which quantifies how likely it is to substitute one amino acid with the other. The amino acid mutants in the ancestral structure are also shown using the bond and atom representation.

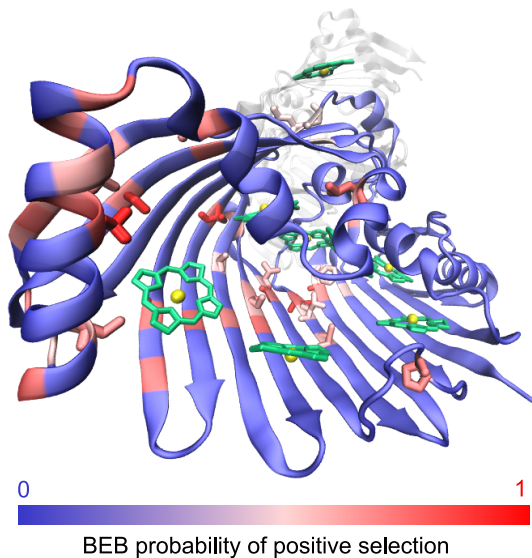


Figure 5. Positively selected sites shown in the structure of *C. tepidum* (PDB: 3ENI). The color gradient corresponds to the strength of positive selection (darkest red - strongest selection, blue - no positive selection). We only plot the side chains of positively selected residues which are within 6 Å of the magnesium in the BChl molecules.

tra.

### Coherence and 2D spectra

Using the hierarchy equation of motion (HEOM) non-Markovian master equation method [32–34], we computed the 2D-echo spectra of the reconstructed ancestral FMO complex and of *C. tepidum* at 150 K. To this end we employed the *QMaster* software package [35] (for more details see Methods). The spectral densities which were employed are described in Methods. These were obtained by fitting the original QM/MM spectral densities to Drude-Lorentz spectral densities with three peaks. The spectral densities indicated a similar coupling strength of the system to the bath for the ancestral and *C. tepidum* FMO complexes for almost all modes. The total signal of the 2D-echo spectra, i.e. sum of the stimulated emission (SE), ground state bleaching (GB), and excited state absorption (ESA) pathways is shown in Fig. 8. From the oscillations of the cross-peaks in panel B) we cannot deduce an improvement in quantum coherence or a significant difference between the ancestor and *C. tepidum*. For all species, cross-peak beatings in the 2D-echo spectra are dominated by ground state vi-



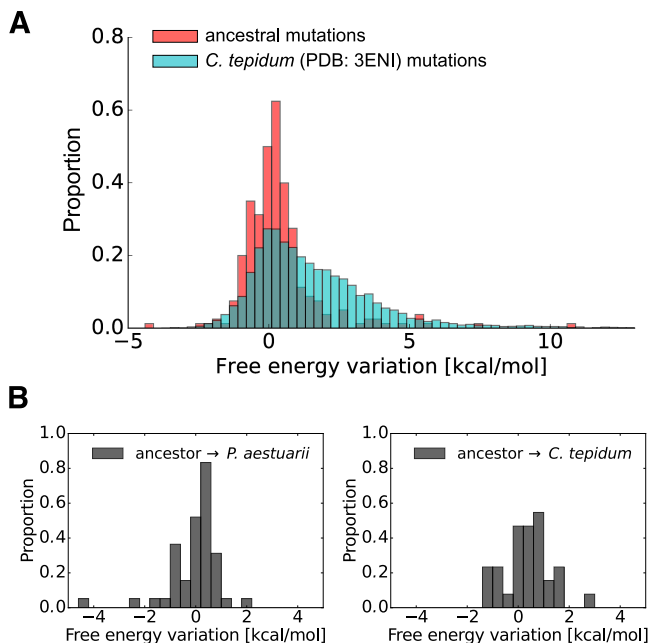


Figure 6. Panel **A**: In blue we show a histogram of the folding free energy changes for all possible single point mutations of the current day *C. tepidum* FMO complex structure. In red, we show a histogram of the folding free energy changes for all the single point mutations which are necessary to connect the ancestral FMO structure to the current day structures (i.e. all single point mutations along all branches). Panel **B**: Right-hand side: histogram of the folding free energy changes for the mutations which connect *P. aestuarii* to the ancestor. Left-hand side: histogram of the folding free energy changes for the mutations which connect *C. tepidum* to the ancestor. Note that, for all histograms, each bin contains the number of points with energy in that interval normalized by the area under the entire histogram.

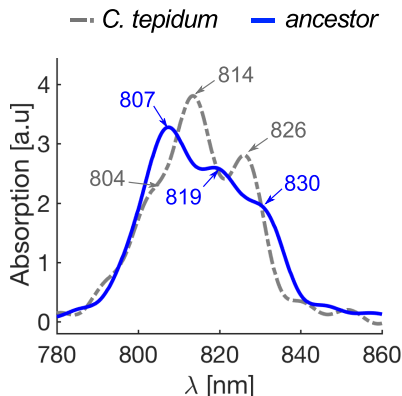


Figure 7. Comparison of simulated absorption spectra of the ancestral FMO complex (blue line) to that of current day *C. tepidum* at 300K (grey dashed line) in arbitrary units. Spectra were computed using the Qy transitions obtained by using QM/MM. See Methods for more details.

brations [36] superposed by minor vibronic contributions. This suggests that optimizing exciton transport through quantum coherence was not part of the evolution of the FMO complex.

## CONCLUSION

We have reconstructed a structure for the ancestral Fenna-Matthews-Olson complex and found that mutations of its amino acids over time have influenced the free energy upon folding of the protein complex. In particular, the current day specie of *P. aestuarii* was obtained through stabilizing mutations while that of *C. tepidum* is less stable than the ancestor. Regarding exciton transport, we do not observe a significant change or improvement in the efficiency of exciton transport or quantum coherent transport. These results suggest that the complex did not evolve to optimize for quantum coherent transport. It is also possible that the ancestor was already sufficiently optimized for exciton transport and therefore further evolution or optimization was not necessary. One of the results we find is that mutations most likely led to better binding of the FMO complex to the baseplate and reaction center. This is confirmed by the larger instability associated with mutating residues in those locations. This leaves an open question: perhaps the overall exciton transport, from the chlorosome to the reaction center, was optimized by favoring mutations in FMO which led to a stronger binding of FMO to its neighbouring protein systems.

For future work, we are interested in looking at the exciton transport at each node of the phylogenetic tree and further in expressing the ancestral sequence in current day *C. tepidum* to obtain an experimental structure and 2D-echo spectra for the ancestor. Finally it would be interesting to look at the role of photoprotection to see whether the mutations could have influenced it.

## METHODS AND COMPUTATIONAL DETAILS

### Stability of the *C. tepidum* and *P. aestuarii* Fenna-Matthews-Olson complex to mutations

Each of the amino acids of the trimer and monomer of the FMO complex of *P. aestuarii* and *C. tepidum* were mutated to the each of the other possible 19 amino acids using FoldX [26]. The corresponding free energy variation upon folding  $\Delta\Delta G = \Delta G_{mut} - \Delta G_{wt}$  was obtained for each mutation. In order to account for the effect of mutations at the interface between monomers within the trimer, the mutations were carried out simultaneously in each monomer of the trimer and the resulting free energy variation was normalized by dividing by three.

In FoldX, mutations are modeled as follows. The initial crystal structure is optimized to remove any eventual

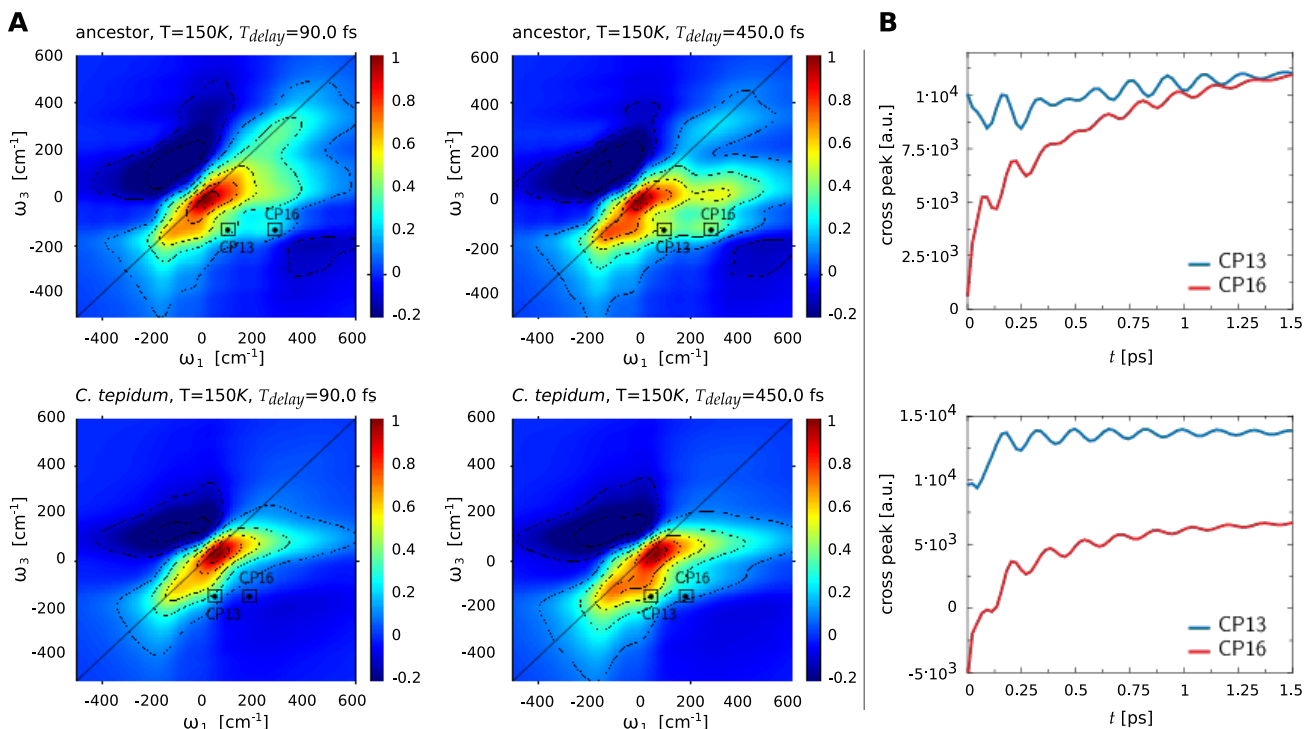


Figure 8. Panel **A**: Contour plots of the total computed signal for the 2D-echo spectra at different delay times. The figures in the top row show results for the ancestor at a delay time of 90 and 400 fs and the bottom figures show the analogous plots for *C. tepidum*. Panel **B**: The amplitude of oscillation of two specific cross peaks. The top image is for the ancestor and the bottom image is for *C. tepidum*.

steric clashes. Then, the residue of interest is mutated and its nearest neighbors are mutated to themselves and conformationally relaxed to remove any local clash. The nearest neighbors are mutated to themselves so that their geometry may be optimized together with that of the central residue. During this procedure the backbone of the protein is kept fixed and all other residues that are far from the one of interest are also kept fixed. The stability,  $\Delta G_{wt}$ , of this relaxed structure is obtained by using an effective energy function. Subsequently, the residue of interest is mutated to each of the other 19 amino acids and its neighbors to themselves and the various  $\Delta G_{mut}$  are computed.

The procedure described above was repeated 5 times for each mutation to ensure that the minimum energy conformations of large residues that have many rotamers were identified. The effective energy function (“effective energy” here refers to the Helmholtz free energy of a system (protein + solvent) for a fixed protein conformation) in FoldX has been optimized for amino acid sequences, thus all BChl-*a* molecules could not be included directly in this calculation. To account for their presence, the structures given in input to FoldX were obtained by homology modeling with Modeller [37]. In the Modeller simulations, the BChl molecules were inserted and kept fixed as hard spheres. In the FoldX optimization the residues that are known to bind to BChl-*a* molecules from the crystal structure analysis of FMO complexes

from current day species were also kept fixed. A similar procedure was recently employed successfully for the case of RubisCO where Mg atoms are present [38].

### Determination of positively selected sites: site and branch-site models

#### Phylogenetic tree

All *fmoA* gene sequences from the EMBL database were gathered and employed to generate an alignment using translatorX with MAFFT [29]. Phylogenetic trees were constructed using PhyML [30] with 5000 bootstraps. The parameters and settings used in PhyML were as following. The LG substitution model was chosen. We selected to have four substitution rate categories. The alpha parameter for the gamma distribution of sites was set to be estimated by the code. Both NNIs and SPR methods were used to search for the optimal tree topology and finally, tree topology, branch lengths and rate parameters were chosen to be optimized by the code. A set of three trees were constructed. In the first tree, all sequences were included excluding FJ210646, as it was missing about 100 residues. Therefore, including it would have introduced more error in the tree reconstruction phase. For the second tree, we removed *Chloroacidobacterium thermophilum* (ABV27353) as it had the lowest

sequence identity percent and thus also introduced more uncertainty. In the third tree, *Chloroherpeton thalassium* (ACF13179) was removed as it was the second most distant sequence from the rest. We computed ancestral sequences and searched for positively selected sites on all three trees but we present results for the third tree as we believe it has the smallest error.

### Site and branch-site models

The branches under positive selection were identified using the branch-site model [39] as implemented in CodeML. This model allows for variation of  $\omega = \frac{dN}{dS}$  (the ratio of synonymous to non synonymous mutations) amongst branches and sites. For each simulation, one branch is selected as a foreground branch and, using CodeML, we computed the likelihood that the branch was under positive selection. The input DNA sequence alignment was the same as the one generated to deduce the phylogenetic tree. Given a branch under positive selection, we determined which amino acids were under positive selection by using the Bayes Empirical Bayes (BEB) model [40]. We corrected the probability values p-values for False Discovery Rate (FDR) by using the q-value [41], as discussed in Ref. [42].

## Reconstruction of the ancestral protein structure of FMO

### Sequence reconstruction

An ancestral sequence was reconstructed using maximum likelihood as implemented in FastML [43] and the LG+G model for amino acid substitution. The LG+G model was established to be the best model under the Bayesian Information Criterion (BIC). With FastML, we obtained the most probable sequences, together with the posterior probabilities for each character and indel at each sequence position for each internal node of the tree. As inputs, we used the phylogenetic trees described in the previous section and rooted them based on the most distant sequence. The alignments used in the input were the same as those employed to generate the trees. For the last tree that excludes *C. thermophilum* and *C. thalassium*, we used the midpoint root, as most sequences are similar, (see Fig. 3) and the branching is almost identical to that obtained when *C. thalassium* or *C. thermophilum* are included.

### Structure reconstruction and molecular dynamics

The ancestral structure was built by using homology modeling with satisfaction of spatial restraints as implemented in Modeller [37]. The method of modeling by satisfaction of spatial restraints works as follows. Constraints are generated on the structure of the target se-

quence using its alignment to the related protein structures as a guide. The restraints are obtained based on the assumption that the structures will be similar in the aligned regions. In MODELLER, the form of the restraints was obtained from a statistical analysis of the relationships between similar protein structures in a database of 105 alignments that included 416 proteins of known 3D structure [37]. These restraints are supplemented by stereochemical restraints such as bond lengths, angles etc, which are obtained from a force field. Once all these restraints are established, the model structure is obtained in Cartesian space by minimizing the violations of all restraints.

We used the structure of *P. aestuarii* (PDB: 3EOJ) as the homologue and generated 100 possible structures with slow refinement. The ancestral structure was chosen to be the one with the best molpdb factor. The initially reconstructed structure only included the protein scaffold, as there is no current parametrization for BChl's in Modeller. Thus, BChl molecules were included subsequently using minimization as implemented in NAMD [44]. The chromophores were initially positioned as in the homologous structure and the structure was optimized by minimizing the energy in two steps. In the first step, the backbone was kept fixed, and for the second minimization the backbone was free to move. The structure was subsequently equilibrated without constraints using the Amber14 software package, [45] with the Amber ff99SB force field[46]. The BChl-a parameters employed are reported in Refs. [11, 47]. The protonation states of all amino acids were determined with the H++ 3.0 software [48], under neutral pH conditions. All complexes were solvated using TIP3P periodic water boxes, [49] with a minimum distance of 15 Å between the complex and the box boundaries. Charges were neutralized by adding sodium ions for the ancestor and *P. aestuarii* and chloride for *C. tepidum*. Shake constraints were applied to all bonds containing hydrogen. Minimizations were carried out for 2000 steps for *P. aestuarii* and *C. tepidum* and for 10000 steps for the ancestor. Minimizations were followed by 200 ps adaptation runs to impose a temperature of 300 K and a pressure of 1 atm on the systems. All three complexes were equilibrated for 50 ns in the same environmental conditions. Long range electrostatic interactions were calculated using the Particle-Mesh Ewald method [50]. For each complex we then carried out 40 ps production runs with a 1 fs integration step.

## Correlating biological stability and evolution to exciton dynamics

### QM/MM Hamiltonian

For the exciton dynamics, the FMO complex is simulated as a system coupled to a bath (the protein environ-



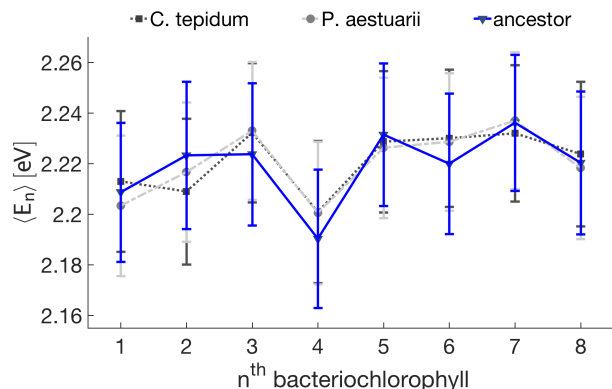


Figure 9. Average first excited state energies  $\langle E_n \rangle$  for each BChl molecule in the FMO complex of *C. tepidum* (black), *P. aestuarii* (grey) and for the ancestral structure (blue). Values were obtained by averaging over the production QM/MM trajectory at 300K.

ment). The system Hamiltonian is defined as

$$H_{\text{ex}} = \sum_{i=1}^8 \varepsilon_i |i\rangle\langle i| + \sum_{i \neq j}^8 V_{ij} |i\rangle\langle j| \quad (1)$$

where  $\varepsilon_i$  is the first excited state energy of the  $i$ -th BChl. The  $V_{ij}$  terms correspond to the excitonic coupling between the excited states for the  $i$ -th and  $j$ -th molecule.

Site energies were computed using TDDFT in QChem [51] with the PBE0 functional [52] and 3-21G basis set for 10000 frames (40 ps) of the MD production run. Couplings were calculated using two approaches: the point-dipole approximation (PDA) and via transition charges from the electrostatic potential (TrEsp) [53]. TrEsp has shown to be the most accurate, although it is computationally more demanding than using the PDA [53]. The computed couplings are given in the Supplementary information.

The average first excited state energy of each BChl is shown in Fig. 9. We notice there is no large change in the trend of the excited state energies for the BChl's.

### Exciton coherence and 2d spectrum

The 2d-echo spectra in Fig. 8 were calculated as in Ref. [54]. In two-dimensional electronic spectroscopy the sample is probed by a sequence of three laser pulses. Adjusting the delay time  $T_{\text{delay}}$  between the second and the third pulse yields a time resolved picture of the exciton dynamics. Within the impulsive limit (assuming  $\delta$ -pulses), the 2D-echo spectrum is related to the third

order response function  $S^{(3)}(t_1, T_{\text{delay}}, t_3)$ . Phase matching ensures that the components of the detected signal go along distinct directions, and thus can be experimentally separated. We considered the rephasing (RP) component of the signal

$$I_{RP}(\omega_1, T_{\text{delay}}, \omega_3) = \dots \quad (2)$$

$$\iint_0^{\infty} dt_1 dt_3 e^{i\omega_3 t_3 - i\omega_1 t_1} S_{RP}^{(3)}(t_1, T_{\text{delay}}, t_3)$$

for which coherent phenomena show as unique oscillatory pattern in the cross-peak dynamics as a function of delay time. Using the notation of double sided Feynman diagrams [55, 56], the total signal is given by three separate pathways: stimulated emission (SE), ground state bleaching (GB) and excited state absorption (ESA). The latter involves the double exciton manifold. We numerically evaluated  $I_{RP}(\omega_1, T_{\text{delay}}, \omega_3)$  by propagating the reduced density matrix, describing the exciton degrees of freedom, along the double sided Feynman diagrams. Hereby, each interaction with the laser pulses requires an interruption of the dynamics and a multiplication of the reduced density matrix with the dipole operator, either from the right or from the left. The propagation was done using *QMaster* [35], a high-performance implementation of HEOM [57, 58]. The rotational average over random orientations of the probed sample was included by sampling 20 laser polarization vectors aligned with the vertices of a dodecahedron [54].

## ACKNOWLEDGEMENTS

S. V. would like to thank Pouria Dasmeh and Adrian Serohijos for their interesting discussions on methods to compute the free energy changes for mutations and phylogenetic tree reconstruction. The authors thank Nicolas Sawaya for sharing his code for the calculation of atomic partial charges from the transition densities. The computations in this paper were completed on the Odyssey cluster supported by the FAS Division of Science, Research Computing Group at Harvard University. S. V., F. H. and A. A.-G. acknowledges support from the Center for Excitonics, an Energy Frontier Research Center funded by the U.S. Department of Energy, Office of Science and Office of Basic Energy Sciences under Award Number de-sc0001088. A.A.G. acknowledges the generous support from the Canadian Institute for Advanced Research. This work was supported as part of the Photosynthetic Antenna Research Center (PARC), an Energy Frontier Research Center funded by the U.S. Department of Energy, Office of Science, Office of Basic Energy Sciences under Award Number de-sc 0001035 to REB. RS was supported by the PARC grant.

[1] J. J. Brocks, G. D. Love, R. E. Summons, A. H. Knoll, G. A. Logan, and S. A. Bowden, *Nature* **437**, 866 (2005).

[2] R. E. Blankenship, (Wiley-Blackwell, Oxford, UK, 2014).

- [3] J. Adolphs and T. Renger, *Biophys. J.* **91**, 2778 (2006).
- [4] M. Mohseni, P. Rebentrost, S. Lloyd, and A. Aspuru-Guzik, *J. Chem. Phys.* **129**, 174106 (2008).
- [5] P. Rebentrost, M. Mohseni, I. Kassal, S. Lloyd, and A. Aspuru-Guzik,.
- [6] A. Ishizaki and G. R. Fleming, *Proc. Natl Acad. Sci. USA.* **106**, 17255 (2009).
- [7] P. Rebentrost, M. Mohseni, and A. Aspuru-Guzik, *J. Phys. Chem. B.* **113**, 9942 (2009).
- [8] G. Panitchayangkoon, D. Hayes, K. A. Fransted, J. R. Caram, E. Harel, J. Wen, R. E. Blankenship, and G. S. Engel, *Proc. Natl Acad. Sci. USA.* **107**, 12766 (2010).
- [9] P. Rebentrost, S. Shim, J. Yuen-Zhou, and A. Aspuru-Guzik, *Procedia Chemistry* **3**, 332 (2011).
- [10] G. Ritschel, J. Roden, W. T. Strunz, A. Aspuru-Guzik, and A. Eisfeld, *J. Phys. Chem. Lett.* **2**, 2912 (2011).
- [11] S. Shim, P. Rebentrost, S. Valteau, and A. Aspuru-Guzik, *Biophys. J.* **102**, 649 (2012).
- [12] S. Valteau, A. Eisfeld, and A. Aspuru-Guzik, *J. Chem. Phys.* **137**, 224103 (2012).
- [13] J. Dostlál, J. Pšenčík, and D. Zigmantas, *Nat. Chem.* (2016), 10.1038/nchem.2525.
- [14] G. S. Engel, T. R. Calhoun, E. L. Read, T.-K. Ahn, T. Mancal, Y.-C. Cheng, R. E. Blankenship, and G. R. Fleming, *Nature.* **446**, 782 (2007).
- [15] G. D. Scholes, G. R. Fleming, L. X. Chen, A. Aspuru-Guzik, A. Buchleitner, D. F. Coker, G. S. Engel, R. van Grondelle, A. Ishizaki, D. M. Jonas, J. S. Lundeen, J. K. McCusker, S. Mukamel, J. P. Ogilvie, A. Olaya-Castro, M. A. Ratner, F. C. Spano, K. B. Whaley, and X. Zhu,.
- [16] F. Fassioli and A. Olaya-Castro,.
- [17] C. Kreisbeck and T. Kramer, *J. Phys. Chem. Lett.* **3**, 2828 (2012).
- [18] A. Olaya-Castro, C. Lee, F. Olsen, and N. Johnson, *Phys. Rev. B.* **78**, 085115 (2008).
- [19] C. Olbrich, T. L. C. Jansen, J. Liebers, M. Aghtar, J. Strümpfer, K. Schulten, J. Knoester, and U. Kleinekathöfer, *J. Phys. Chem. B* **115**, 8609 (2011).
- [20] J. Wen, Y. Tsukatani, W. Cui, H. Zhang, M. L. Gross, D. A. Bryant, and R. E. Blankenship, *BBA - Bioenergetics* **1807**, 157 (2011).
- [21] J. M. Olson,.
- [22] R. G. Saer, V. Stadnytskyi, N. C. Magdaong, C. Goodson, S. Savikhin, and R. E. Blankenship, *Biochimica et Biophysica Acta (BBA) - Bioenergetics* **1858**, 288 (2017).
- [23] R. Saer, G. S. Orf, X. Lu, H. Zhang, M. J. Cuneo, D. A. Myles, and R. E. Blankenship, *BBA - Bioenergetics* **1857**, 1455 (2016).
- [24] F. Müh, M. E.-A. Madjet, J. Adolphs, A. Abdurahman, B. Rabenstein, H. Ishikita, E.-W. Knapp, and T. Renger, *Proc. Natl. Acad. Sci. U. S. A.* **104**, 16862 (2007).
- [25] D. E. Tronrud, J. Wen, L. Gay, and R. E. Blankenship, *Photosynth. Res.* **100**, 79 (2009).
- [26] R. Guerois, J. E. Nielsen, and L. Serrano, *J. Mol. Bio.* **320**, 369 (2002).
- [27] K. B. Zeldovich, P. Chen, and E. I. Shakhnovich, *Proceedings of the National Academy of Sciences* **104**, 16152 (2007).
- [28] N. Tokuriki, F. Stricher, J. Schymkowitz, L. Serrano, and D. S. Tawfik, *Journal of Molecular Biology* **369**, 1318 (2007).
- [29] F. Abascal, R. Zardoya, and M. J. Telford,.
- [30] S. Guindon, J.-F. Dufayard, V. Lefort, M. Anisimova, W. Hordijk, and O. Gascuel, *Systematic Biology* **59**, 307 (2010).
- [31] J. Olson, K. Bacon, and K. H. Thompson,.
- [32] Y. Tanimura and R. Kubo,.
- [33] A. Ishizaki and Y. Tanimura,.
- [34] A. Ishizaki and G. R. Fleming, *J. Chem. Phys.* **130**, 234111 (2009).
- [35] C. Kreisbeck, T. Kramer, and A. Aspuru-Guzik,.
- [36] C. Kreisbeck, T. Kramer, and A. Aspuru-Guzik, *J. Phys. Chem. B* **117**, 9380 (2013).
- [37] A. Sali and T. L. Blundell,.
- [38] R. A. Studer, P. A. Christin, M. A. Williams, and C. A. Orengo, *Proc. Natl. Acad. Sci.* **111**, 2223 (2013).
- [39] J. Zhang, R. Nielsen, and Z. Yang, *Mol. Biol. Evol.* **22**, 2472 (2005).
- [40] Z. Yang, W. S. Wong, and R. Nielsen, *Mol. Biol. Evol.* **22**, 1107 (2005).
- [41] D. A. Bass JDSwcfAJ and R. D,.
- [42] M. Anisimova and Z. Yang, *Mol. Biol. Evol.* **24**, 1219 (2007).
- [43] H. Ashkenazy, O. Penn, A. Doron-Faigenboim, O. Cohen, G. Cannarozzi, O. Zomer, and T. Pupko, *Nucleic Acids Res.* **40**, W580 (2012).
- [44] J. C. Phillips, R. Braun, W. Wang, J. Gumbart, E. Tajkhorshid, E. Villa, C. Chipot, R. D. Skeel, L. KalÁĀ, and K. Schulten, *Journal of Computational Chemistry* **26**, 1781 (2005).
- [45] D. A. Case, V. Babin, J. T. Berryman, R. M. Betz, Q. Cai, D. S. Cerutti, T. E. Cheatham III, T. A. Darden, R. E. Duke, H. Gohlke, A. W. Goetz, S. Gusarov, N. Homeyer, P. Janowski, J. Kaus, I. Kolossváry, A. Kovalenko, T. S. Lee, S. LeGrand, T. Luchko, R. Luo, B. Madej, K. M. Merz, F. Paesani, D. R. Roe, A. Roitberg, C. Sagui, R. Salomon-Ferrer, G. Seabra, C. L. Simmerling, W. Smith, J. Swails, R. C. Walker, J. Wang, R. M. Wolf, X. Wu, and P. A. Kollman, (2014).
- [46] T. E. Cheatham, R. Cieplak, and R. A. Kollman,.
- [47] S. Chandrasekaran, M. Aghtar, S. Valteau, A. Aspuru-Guzik, and U. Kleinekathöfer, *J. Phys. Chem. B* **119**, 9995 (2015), pMID: 26156758.
- [48] R. Anandakrishnan, B. Aguilar, and A. V. Onufriev,.
- [49] W. L. Jorgensen and J. D. Madura,.
- [50] U. Essmann, L. Perera, M. L. Berkowitz, T. Darden, H. Lee, and L. Pederson,.
- [51] Y. Shao, L. F. Molnar, Y. Jung, J. Kussmann, C. Ochsenfeld, S. T. Brown, A. T. Gilbert, L. V. Slipchenko, S. V. Levchenko, D. P. O'Neill, R. A. DiStasio Jr, R. C. Lochan, T. Wang, G. J. Beran, N. A. Besley, J. M. Herbert, C. Yeh Lin, T. Van Voorhis, S. Hung Chien, A. Sodt, R. P. Steele, V. A. Rassolov, P. E. Maslen, P. P. Korambath, R. D. Adamson, B. Austin, J. Baker, E. F. C. Byrd, H. Dachsel, R. J. Doerksen, A. Dreuw, B. D. Dunietz, A. D. Dutoi, T. R. Furlani, S. R. Gwaltney, A. Heyden, S. Hirata, C.-P. Hsu, G. Kedziora, R. Z. Khalliulin, P. Klunzinger, A. M. Lee, M. S. Lee, W. Liang, I. Lotan, N. Nair, B. Peters, E. I. Proynov, P. A. Pieniazek, Y. Min Rhee, J. Ritchie, E. Rosta, C. David Sherrill, A. C. Simmonett, J. E. Subotnik, H. Lee Woodcock III, W. Zhang, A. T. Bell, A. K. Chakraborty, D. M. Chipman, F. J. Keil, A. Warshel, W. J. Hehre, H. F. Schaefer III, J. Kong, A. I. Krylov, P. M. W. Gill, and M. Head-Gordon, *Phys. Chem. Chem. Phys.* **8**, 3172 (2006).

- [52] J. P. Perdew, M. Ernzerhof, and K. Burke, *J. Chem. Phys.* **105**, 9982 (1996).
- [53] M. E. Madjet, A. Abdurahman, and T. Renger,.
- [54] B. Hein, C. Kreisbeck, T. Kramer, and M. Rodriguez,.
- [55] S. Mukamel, (Oxford: Oxford University Press, 1999).
- [56] M. Cho, (Boca Raton, FL: CRC Press, 2009).
- [57] C. Kreisbeck, T. Kramer, M. Rodríguez, and B. Hein,.
- [58] C. Kreisbeck and T. Kramer, (2013), 10.4231/D3RB6W248.
- [59] T. Renger, M. E.-A. Madjet, M. Schmidt am Busch, J. Adolphs, and F. Müh, *Photosynth. Rev.* **116**, 367 (2013).
- [60] B. H. Besler, K. M. Merz, and P. A. Kollman, *J. Comput. Chem.* **11**, 431 (1990).
- [61] E. Sigfridsson and U. Ryde, *J. Comput. Chem.* **19**, 377 (1998).
- [62] M. M. Francl, C. Carey, L. E. Chirlian, and D. M. Gange, *J. Comput. Chem.* **17**, 367 (1996).
- [63] S. I. E. Vulto, S. Neerken, R. J. W. Louwe, M. A. de Baat, J. Amesz, and T. J. Aartsma, *J. Phys. Chem. B.* **102**, 10630 (1998).

## SUPPORTING INFORMATION (SI)

### Phylogenetic tree

In Fig. S1 we show the phylogenetic tree of the FMO complex, based on the *fmoA* gene, with branch lengths defined in terms of sequence identity.

### Thermodynamic results

In Fig. S2 we compare the free energy variation histograms for *P. aestuarii* and *C. tepidum*. We notice that the distributions are not significantly different. This was also checked by a Kolmogorov-Smirnov goodness-of-fit test.

Free energy changes due to mutations vary depending on the location in the protein complex monomers of *P. aestuarii* and *C. tepidum*. We found that mutations at the interface of monomers are destabilizing. We identify regions where mutations are more stabilizing (green box) and regions where they are mostly destabilizing (black box). In the top left panel of Fig. S3 we show that the outer amino acids neighboring the 8-th BChl can be mutated and this causes no stress / very little stress to the structure. On the other hand, in the top right panel, we show that it is much more destabilizing to mutate the inner alpha-helix (black box), which lies at the interface with another monomer of the trimer. This could indicate that, in this region, there was a larger priority to stabilize the trimeric shape rather than the interaction with the eight BChl.

### Hamiltonian

Site couplings were computed using the point-dipole approximation (PDA) and the transfer charge from electrostatic potential (TrEsp) method [59].

In the point-dipole approximation, the exciton energy transfer couplings are computed according to Eq. 3, where  $\vec{d}_{10}^A$  denotes the transition dipole of the  $0 \rightarrow 1$  transition for molecule A. Here  $R$  is the distance between the centers of the molecules A and B. To compute the excitation energy transfer couplings in the PDA we assumed an effective dipole strength of  $37.1 \text{ D}^2$ , an orientation of transition dipoles along the axis of the ND and NB nitrogen atoms in the BChls and set  $f = 1$ .

$$V_{10,01}^{\text{PDA}} = \frac{f}{4\pi\epsilon_0} \left( \frac{\vec{d}_{10}^A \cdot \vec{d}_{01}^B}{R^3} - 3 \frac{(\vec{d}_{10}^A \cdot R)(\vec{d}_{01}^B \cdot R)}{R^5} \right) \quad (3)$$

Excitation energy transfer couplings can also be computed from atomic transition charges  $q_i^A(1,0)$  and  $q_j^B(0,1)$  that fit the electrostatic potentials of transition charge densities. We calculated atomic transition charges for all atoms in each of the BChls by fitting the transition

densities. The transition density cube files were obtained using TD-DFT with the 6-31G\* basis set and PBE0 functional in QChem [51]. For the fitting, we employed a method inspired by the Merz-Kollman method [60] and the CHELP-BOW method [61]. A random set of coordinates were chosen, lying more than  $2 \text{ \AA}$  and less than  $8 \text{ \AA}$  from any atom. All points were weighted equally. We avoided all points lying within the van der Waals radius as it has been shown that prioritizing points outside of this radius led to charges that better reproduced the electron density's higher multipoles [61]. A sampling frequency of 6000 points per atom was used.

We used the pseudoinverse method to solve the final system of equations and singular value decomposition to find the pseudo inverse. This approach avoids having to deal with poorly conditioned intermediate matrices [62].

Excitation energy transfer couplings was then computed by summing over the Coulomb potentials between all pairs of atomic transition charges in the two molecules (see Eq. 4)

$$V_{10,01}^{\text{TrEsp}} = \frac{1}{4\pi\epsilon_0} \sum_{i=1}^N \sum_{j=1}^M \frac{q_i^A(1,0)q_j^B(0,1)}{|\vec{r}_i - \vec{r}_j|} \quad (4)$$

Excitation energy transfer couplings for all three FMO complexes calculated in the PDA and with the TrEsp method are reported in Tab. S1.

### Spectral density

We computed two point correlation functions using the QM/MM first excited state energy trajectories obtained for *C. tepidum* and for the ancestor. Subsequently we fourier transformed and employed the harmonic approximation (see Ref. [12]) to obtain the spectral densities  $J(\omega)$ . A spectral density was computed for each BChl for both structures (see Fig. S4). No large difference is seen. We also averaged the spectral densities over all BChl's (see Fig. S5 left panel). The two average spectral densities are almost identical, therefore most changes in the dynamics will originate from changes in the system hamiltonian.

To run the dynamics of the system using the HEOM approach, we fitted the atomistic spectral densities to a three peak Drude-Lorentz spectral density

$$J(\omega) = \sum_{k=1}^3 \left[ \frac{\nu_k \lambda_k \omega}{\nu_k^2 + (\omega + \Omega_k)^2} + \frac{\nu_k \lambda_k \omega}{\nu_k^2 + (\omega - \Omega_k)^2} \right], \quad (5)$$

as done, e.g. in Ref. [36]. The fitted parameters are given in Tab. S3. The fitted spectral densities are shown on the right hand side panels of Fig. S5.

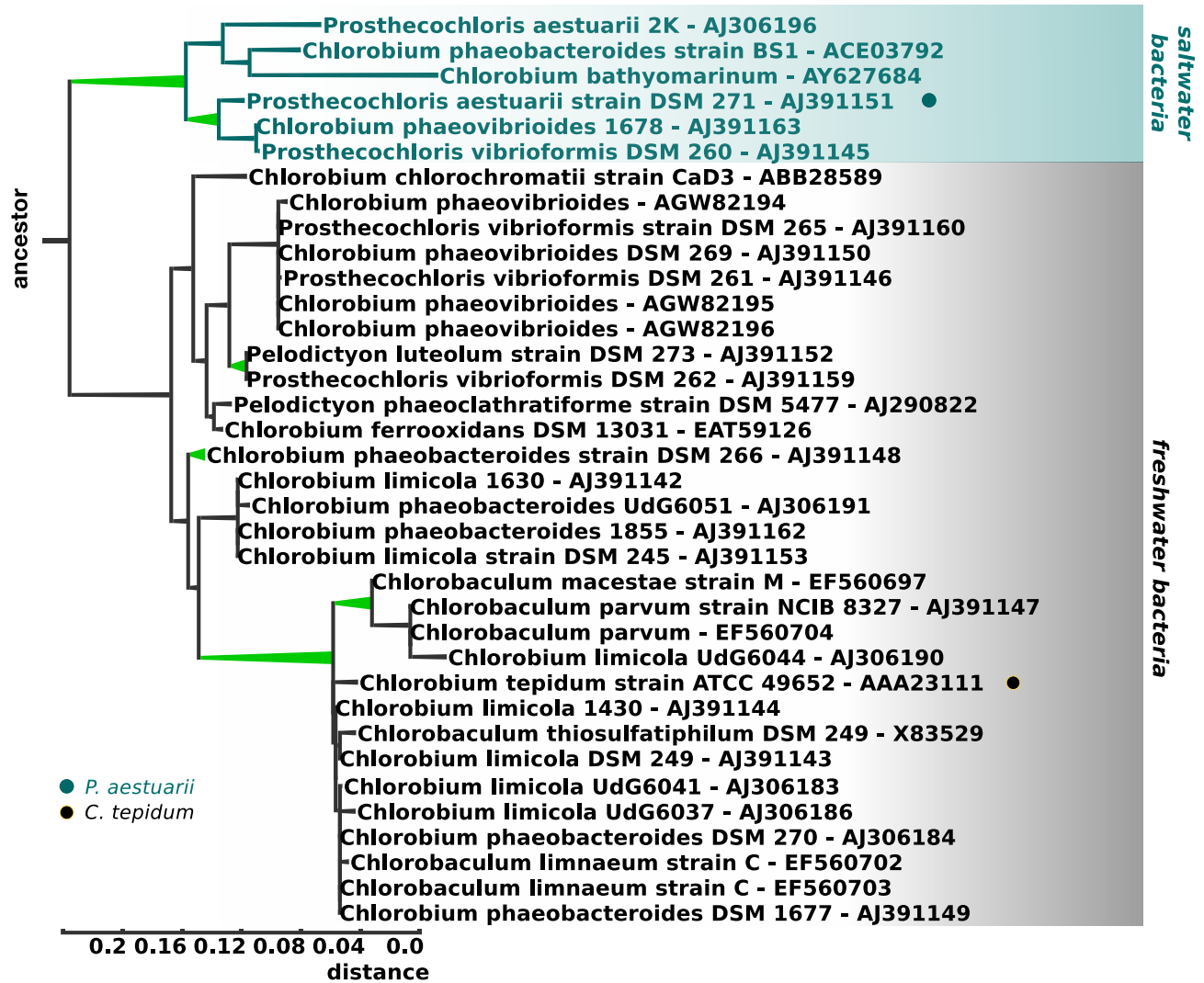


Figure S1. Rooted phylogenetic tree for *fmoA* computed using MAFFT and TranslatorX [29] for the alignment and PHYML [30]. Distances between branches correspond to difference in terms of sequence identity. Branches that are colored in light green are branches where positive selection occurred.



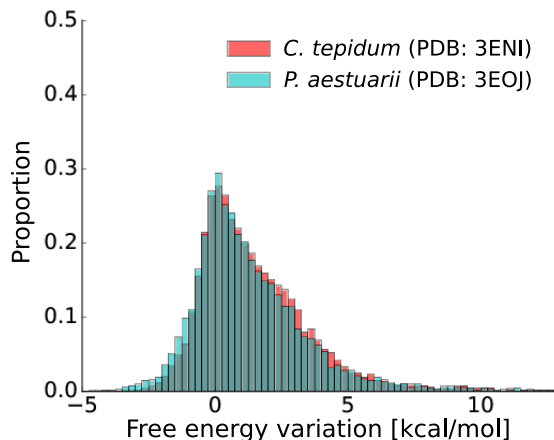


Figure S2. Overlap of free energy variation histograms for all single-point mutations which could be applied to *C. tepidum* (PDB: 3ENI, red) and *P. aestuarii* (PDB: 3EOJ, blue). Each bin contains the number of points with energy in that interval normalized by the area under the entire histogram.

Table S1. Site couplings in *C. tepidum*, *P. aestuarii* and the ancestor in units of  $\text{cm}^{-1}$ . Couplings were computed by using the point-dipole approximation, with  $f = 1$  according to Eq. 3, and also obtained from the transition charge using the electrostatic potential (TrEsp) method, according to Eq. 4.

$H_{nm}$	<i>C. tepidum</i>		<i>P. aestuarii</i>		Ancestor	
	TrEsp [ $\text{cm}^{-1}$ ]	Point dipole [ $\text{cm}^{-1}$ ]	TrEsp [ $\text{cm}^{-1}$ ]	Point dipole [ $\text{cm}^{-1}$ ]	TrEsp [ $\text{cm}^{-1}$ ]	Point dipole [ $\text{cm}^{-1}$ ]
1,2	-133.65	-101.73	-102.28	-92.62	-122.74	-99.83
1,3	-9.53	7.16	-7.89	7.11	-5.53	4.88
1,4	-5.58	-6.27	4.97	-6.49	-6.51	-6.87
1,5	7.99	7.65	8.56	9.17	-9.44	8.54
1,6	-17.05	-15.02	20.83	-34.04	16.27	-23.16
1,7	5.31	-9.38	-11.33	-15.35	-3.05	-8.37
1,8	0.13	-0.04	0.38	0.81	0.08	-0.03
2,3	-39.54	37.13	-39.99	37.48	-37.17	35.63
2,4	9.70	9.26	-9.69	10.92	7.60	8.14
2,5	2.06	2.55	2.11	1.79	-1.80	1.56
2,6	11.27	12.84	-17.60	18.87	-7.25	11.24
2,7	-3.52	-3.66	3.59	3.60	2.60	-11.89
2,8	1.57	1.41	0.79	0.88	2.00	1.98
3,4	124.56	-108.99	-125.38	-129.88	80.99	-81.02
3,5	-4.60	-2.26	1.80	-3.91	-3.41	-5.48
3,6	13.67	-12.17	-11.42	-12.26	-12.23	-12.45
3,7	27.22	20.64	1.79	14.79	7.73	-2.21
3,8	-2.98	2.86	-2.89	2.60	-2.75	2.69
4,5	-85.36	-102.29	103.72	-95.63	115.46	-103.75
4,6	-26.06	-26.00	-25.68	-23.24	27.75	-26.56
4,7	42.09	-66.42	62.51	-62.86	-49.82	-67.90
4,8	-0.86	-2.09	1.90	-2.12	-1.91	-2.36
5,6	103.34	110.91	-86.77	94.11	101.94	115.59
5,7	-2.96	9.09	18.89	9.54	4.87	12.58
5,8	7.25	7.06	7.45	7.15	-7.71	7.28
6,7	-68.02	51.44	-42.72	56.58	-46.75	60.58
6,8	-9.36	-5.36	3.17	-2.33	7.05	-5.57
7,8	9.59	-9.79	-10.38	-9.50	-10.76	-10.21

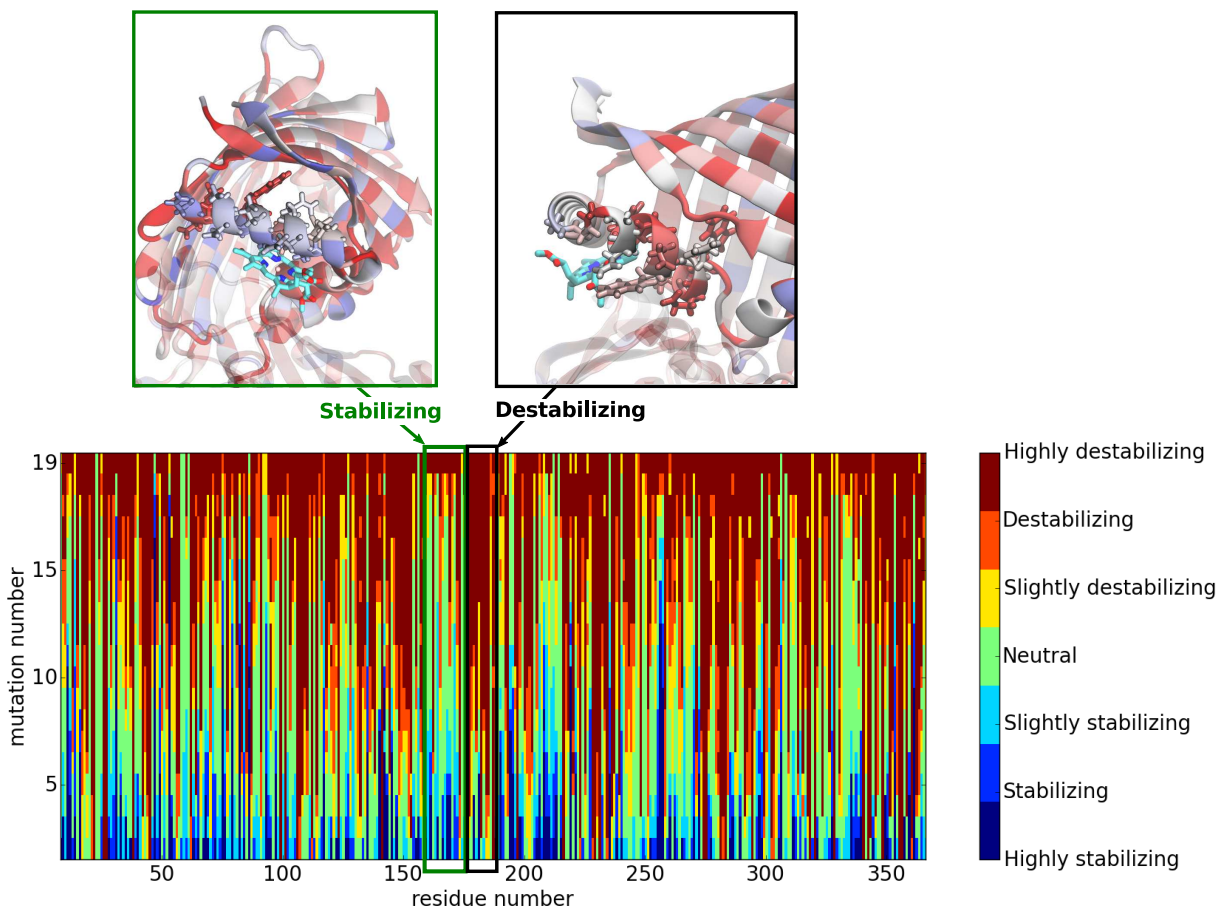


Figure S3. Histogram that summarizes the results of the computed  $\Delta\Delta G$  for all single point mutations in *P. aestuarii*. For each residue number (x-axis) we show a color that represents the free energy change associated with each of the 19 possible single point mutations. The color is selected based on whether the free-energy change is stabilizing or not. Using  $\sigma = 0.46$  kcal/mol, the free energy changes were classified as neutral (green) for  $-\sigma \leq \Delta\Delta G \leq \sigma$ , slightly destabilizing (yellow) for  $\sigma < \Delta\Delta G \leq 2\sigma$ , destabilizing (orange) for  $2\sigma < \Delta\Delta G \leq 3\sigma$  and highly destabilizing (burgundy) for  $3\sigma < \Delta\Delta G$ . Similarly, the stabilizing mutations were classified as  $-2\sigma \geq \Delta\Delta G > -\sigma$  for slightly stabilizing (cyan),  $-3\sigma \geq \Delta\Delta G > -2\sigma$  for stabilizing (blue) and  $\Delta\Delta G > -3\sigma$  for highly stabilizing (navy). On the top left-hand side we show the structure of the alpha-helix near BChl 8, which can be modified in a stabilizing way, and on the right-hand side we highlight neighboring residues in another alpha helix where mutations are more destabilizing.

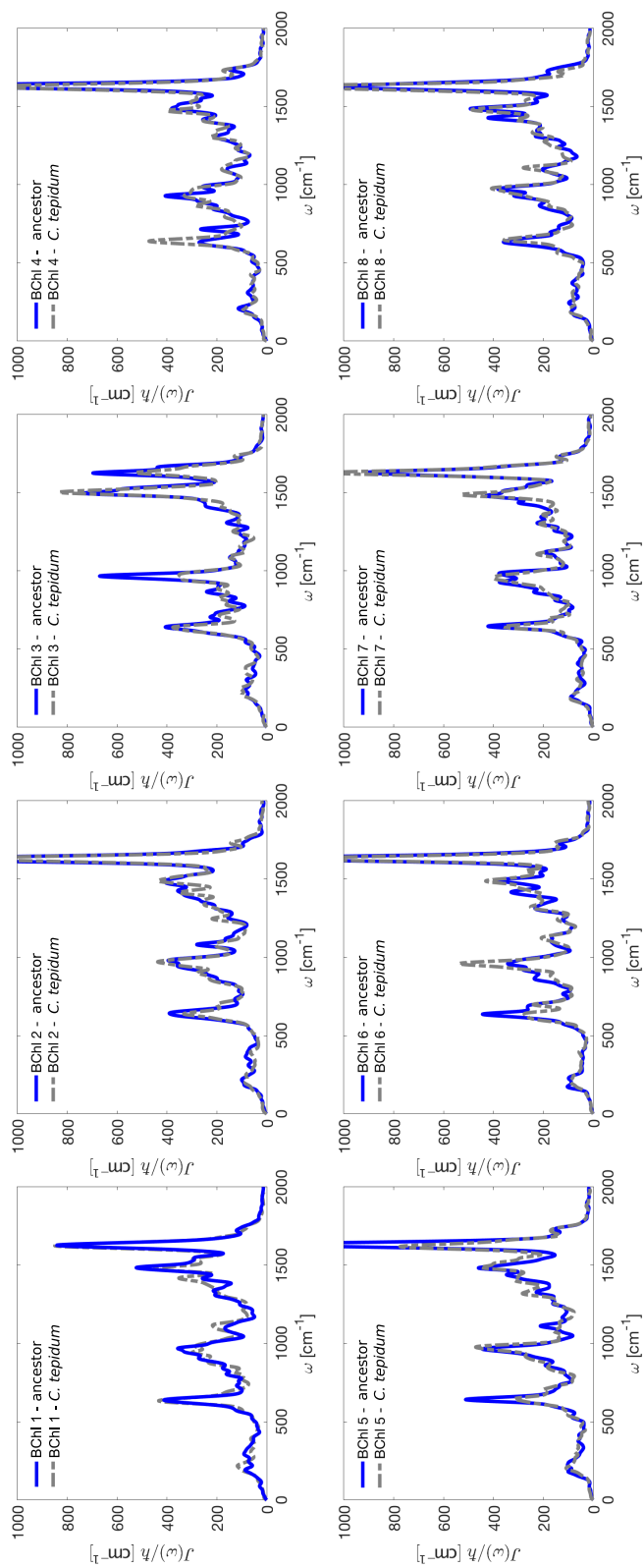


Figure S4. The spectral density,  $J(\omega)$ , of each BChl in the harmonic approximation as a function of frequency. Each plot shows a comparison of the spectral density for the *C. tepidum* FMO complex to that of the ancestral one. No large differences are observed.

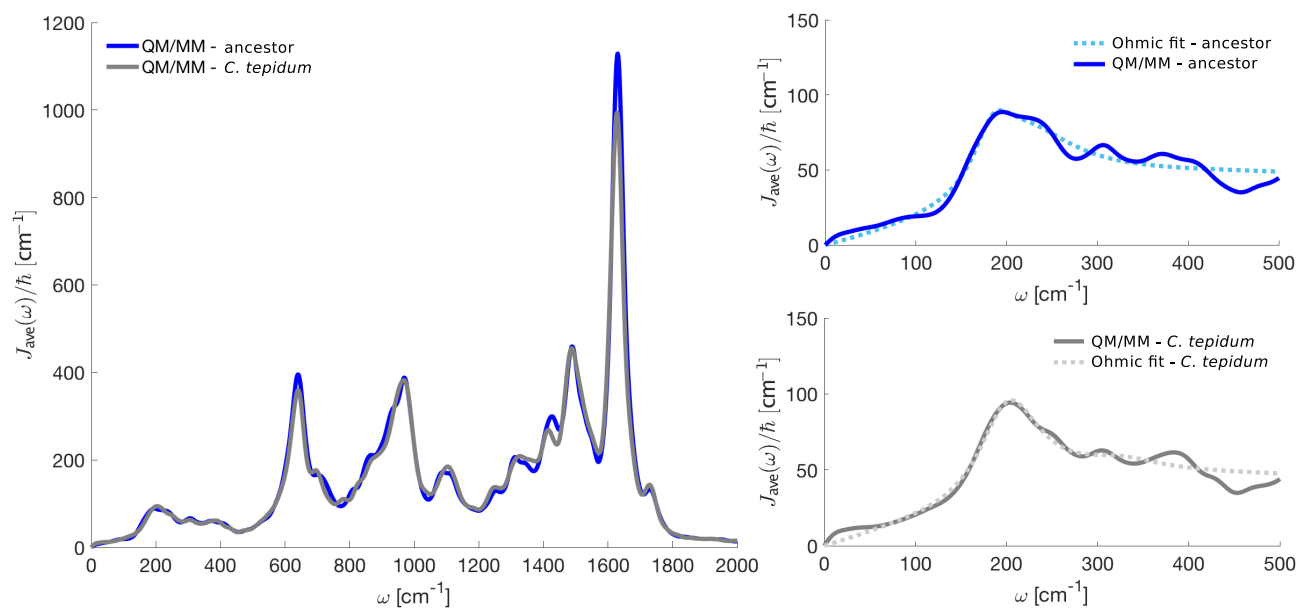


Figure S5. On the left hand side we show the average spectral density for the ancestor and the average spectral density for the *C. tepidum* FMO complex. On the right hand side we show the Ohmic three-peak fit that is taken to obtain the spectral densities used in the HEOM approach for the dynamics. The top panel shows the QM/MM spectral density in a solid line and the Ohmic fit in a dashed line for the ancestral FMO complex. For the bottom panel the spectral densities are shown for *C. tepidum*.

Table S2. Average distances and standard deviations of BChl-protein distance. The distances were computed between Mg atoms for each BChl and their neighboring protein environment. Distances were computed for BChls in *C. tepidum*, *P. aestuarii* and the ancestor. For the protein environment we selected the  $\epsilon$  nitrogen atoms of HIS103, HIS290, HIS283 and HIS138 for sites 1, 3, 4 and 6, the  $\delta$  nitrogens of HIS289 for site 7 and the peptide bond oxygens of TYR234 and TYR116 for sites 5 and 8. Residue indices refer to the *C. tepidum* sequences. Site 2 was not included as it does not bind to the protein scaffold. Distances were computed and averaged over the 40 ps production run.

Average BChl to protein distance $\langle d_{BChl, Protein} \rangle$			
BChl	<i>C. tepidum</i> [Å]	<i>P. aestuarii</i> [Å]	Ancestor [Å]
1	2.81 ± 0.22	2.82 ± 0.31	2.90 ± 0.26
3	4.31 ± 0.37	4.22 ± 0.37	3.89 ± 0.26
4	2.73 ± 0.18	2.58 ± 0.17	2.66 ± 0.22
5	2.47 ± 0.17	2.65 ± 0.21	2.94 ± 0.29
6	2.79 ± 0.24	2.94 ± 0.30	2.59 ± 0.18
7	3.82 ± 0.26	3.85 ± 0.66	3.65 ± 0.30
8	2.23 ± 0.13	2.43 ± 0.16	2.34 ± 0.16

Table S3. Drude-Lorentz parameters used to fit the spectral density for the ancestor and for *C. tepidum*.

	<i>C. tepidum</i>	Ancestor
$1/\nu_1$ [fs]	66.713	66.713
$\lambda_1$ [cm <sup>-1</sup> ]	86.552	72.469
$\Omega_1$ [cm <sup>-1</sup> ]	1.0000	94.462
$1/\nu_2$ [fs]	809.03	506.44
$\lambda_2$ [cm <sup>-1</sup> ]	13.142	11.502
$\Omega_2$ [cm <sup>-1</sup> ]	199.53	215.99
$1/\nu_3$ [fs]	583.76	1229.0
$\lambda_3$ [cm <sup>-1</sup> ]	1.6977	5.1297
$\Omega_3$ [cm <sup>-1</sup> ]	320.78	183.72



### Absorption, CD and LD spectra

In Fig. S6 we show the computed CD and LD spectra for the ancestor and for *C. tepidum* at 300K. In Fig. S7 we show the comparison of our absorption, CD and LD spectra computed using QM/MM results at 300K to the experimental spectra of Ref. [63], for *C. tepidum*. We observe similar peaks in the absorption spectrum although the 300K spectrum is much broader. The fact that the spectrum is broader at 300K is expected because higher temperatures lead to more motion and thus more noise in the system. We also have a similar trend for the CD and LD spectra as that seen experimentally.

### Population dynamics

Using the HEOM approach [32–34] we computed the time evolution of the density matrix of our system of 8

coupled BChl molecules using *QMaster* [35, 58]. The spectral densities were taken to be three peak fits of the atomistic spectral density, as described previously. The resulting population for the ancestor and *C. tepidum* in shown in Fig. S8, we see that site 1 and 2 are less strongly coupled for the ancestor than they are for *C. tepidum*. One can see this also from the Hamiltonians as given in Tab. S1. The coherence between site 1 and 2 is shown in Fig. S9. Here we do not see a large difference between the two species and this further confirms the fact that quantum coherence does not appear to have been selected for.

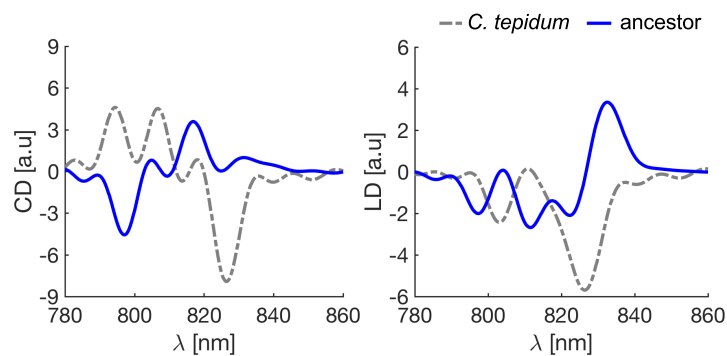


Figure S6. Comparison of simulated CD and LD spectra of the ancestral FMO complex (blue line) to that of current day *C. tepidum* at 300K (grey dashed line) in arbitrary units. Spectra were computed using the Qy transitions obtained by using QM/MM.

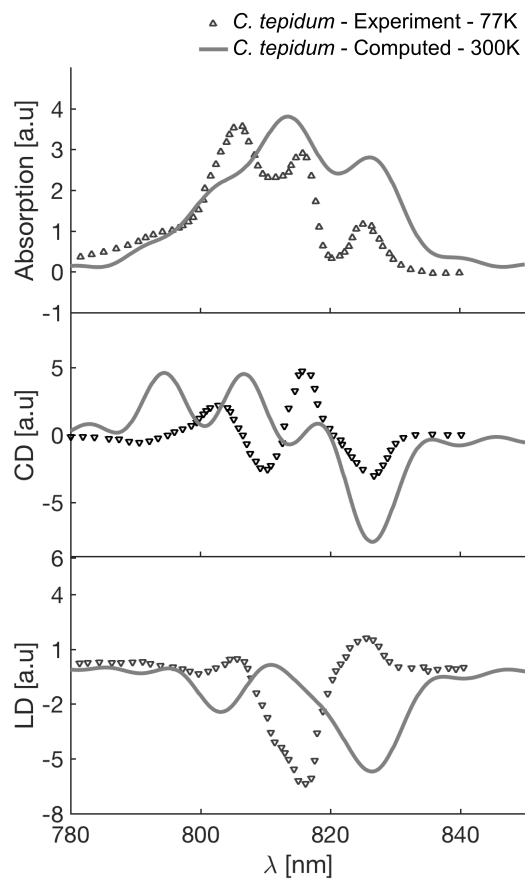


Figure S7. Comparison of our QM/MM spectra to the experimental spectra for *C. tepidum* of Ref. [63].

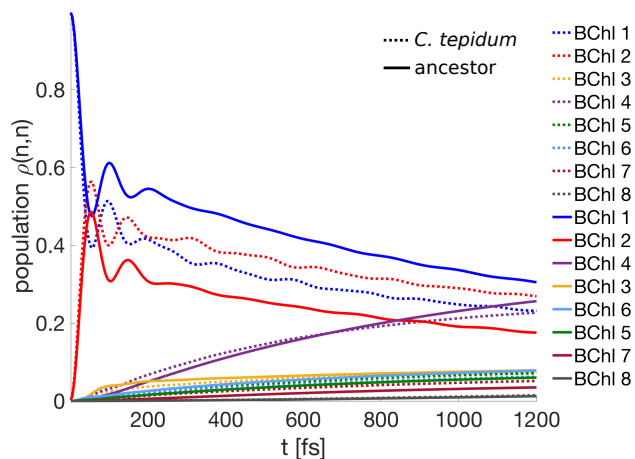


Figure S8. Excited state population of each BChl as a function of time for an initial excited state in BChl 1 (dashed line, *C. tepidum*, solid, Ancestor) at 300K.

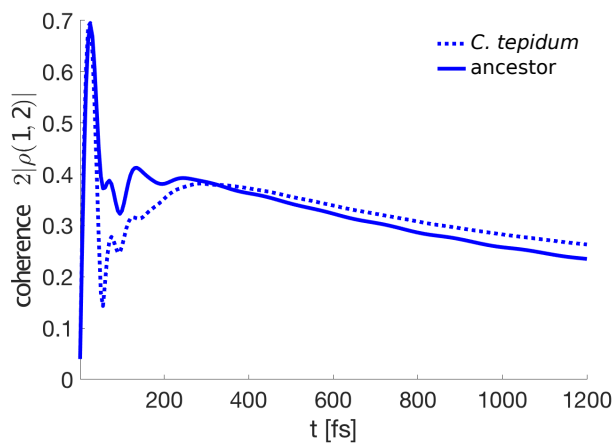


Figure S9. Coherence between the excited states of BChls 1 and 2 as a function of time. These results were obtained by propagating the density matrix of the system using HEOM at 300K and with BChl 1 as the initial state.